THE ASTROPHYSICAL JOURNAL, 541:374–389, 2000 September 20

MOLECULAR ABUNDANCES IN THE ATMOSPHERE OF THE T DWARF Gl 229B

D. SAUMON
Department of Physics and Astronomy, Vanderbilt University, Nashville, TN 37235; dsaumon@cactus.phy.vanderbilt.edu
T. R. GEBALLE
Gemini North Observatory, 670 North A'ohoku Place, Hilo, HI 96720
S. K. LEGGETT
Joint Astronomy Center, 660 North A'ohoku Place, Hilo, HI 96720
M. S. MARLEY
Department of Astronomy, New Mexico State University, Las Cruces, NM 88003
R. S. FREEDMAN
Space Physics Research Institute, NASA Ames Research Center, Moffett Field, CA 94035
K. LODDERS AND B. FEGLEY, JR.
Planetary Chemistry Laboratory, Department of Earth and Planetary Science, Washington University, St. Louis, MO 63130
AND
S. K. SENGUPTA
Department of Physics and Astronomy, Vanderbilt University, Nashville, TN 37235
Received 2000 January 5; accepted 2000 March 21

ABSTRACT

We present new high-resolution infrared spectra of the T dwarf Gliese 229B in the J, H, and K bandpasses. We analyze each of these as well as previously published spectra to determine its metallicity and the abundances of NH_3 and CO in terms of the surface gravity of Gl 229B, which remains poorly constrained. The metallicity increases with increasing gravity and is below the solar value unless Gl 229B is a high-gravity brown dwarf with $\log g$ (cgs) ≈ 5.5. The NH_3 abundance is determined from both the H- and the K-band spectra, which probe two different levels in the atmosphere. We find that the abundance from the K-band data is well below that expected from chemical equilibrium, which we interpret as strong evidence for dynamical transport of NH_3 in the atmosphere. This is consistent with the previous detection of CO and provides additional constraints on the dynamics of the atmosphere of this T dwarf.

Subject headings: stars: abundances — stars: atmospheres — stars: individual (Gl 229B) — stars: low-mass, brown dwarfs

1. INTRODUCTION

Gliese 229B is not only the first brown dwarf recognized as genuine (Nakajima et al. 1995; Oppenheimer et al. 1995), but it is also the brightest and best-studied T dwarf known. With an effective temperature of $T_{\rm eff} \sim 950$ K, it lies squarely between the latest L dwarfs ($T_{\rm eff} \sim 1500$ K; Kirkpatrick et al. (1998)) and the giant planets of the solar system ($T_{\rm eff} \sim 100$ K). Indeed, its near-infrared spectrum shows the strong H_2O absorption bands characteristic of very low mass stars and the strong CH_4 bands seen in the spectra of Jupiter, Saturn and Titan. The transitional nature of the spectrum of Gl 229B is remarkable and hints at the spectral appearance of extrasolar giant planets, which have effective temperatures in the range 200–1600 K (Guillot 1999).

A wealth of data on Gl 229B has accumulated since its discovery five years ago. Broadband photometry from R through N and an accurate parallax (Matthews et al. 1996; Golimowski et al. 1998; Leggett et al. 1999; Perryman et al. 1997) allow an accurate determination of its bolometric luminosity. Spectroscopic observations (Oppenheimer et al. 1998; Geballe et al. 1996; Schultz et al. 1998) covering the range from 0.8 to 5.0 m have revealed a very rapidly declining flux shortward of 1 μm, the unmistakable presence of CH_4, H_2O, and Cs, and have demonstrated the *absence* of the CrH, FeH, VO, and TiO features characteristic of late M and early L dwarfs. Finally, Noll, Geballe, & Marley (1997) and Oppenheimer et al. (1998) have detected CO with an abundance well above the value predicted by chemical equilibrium, a phenomenon also seen in the atmosphere of Jupiter.

Model spectra for Gl 229B (Marley et al. 1996; Allard et al. 1996; Tsuji, Ohnaka, & Aoki 1996) reproduce the overall energy distribution fairly well and all agree that (1) $T_{\rm eff} \sim 950$ K; (2) compared to gaseous molecular opacity, the dust opacity is small if not negligible in the infrared; and (3) the gravity of Gl 229B is poorly constrained at present. The rapid decline of the flux at wavelengths shortward of 1 μm is interpreted as caused by an absorbing haze of complex hydrocarbons (Griffith, Yelle, & Marley 1998) or alternatively by the pressure-broadened red wing of the K I resonance doublet at 0.77 μm (Tsuji, Ohnaka, & Aoki 1999; Burrows, Marley, & Sharp 2000b).

In this paper, we present new high-resolution spectra in the J, H, and K bands. With the inclusion of the "red" spectrum of Oppenheimer et al. (1998), we analyze each part of the spectrum separately to obtain independent measures of the H_2O abundance of Gl 229B—broadly interpreted as the metallicity index—to detect for the first time the presence of NH_3 in its spectrum, and to estimate the NH_3 abundance at two different depths in the atmosphere. Our results are expressed in terms of the surface gravity, which cannot be determined from the data presented here. Nevertheless, we identify a reduced set of acceptable combinations of $T_{\rm eff}$

and gravity using the observed bolometric luminosity of Gl 229B (Leggett et al. 1999).

The observations and the near-infrared spectra are presented in § 2. Section 3 shows how an accurate parallax, a well-sampled spectral energy distribution, and evolutionary models greatly reduce the possible range of combinations of $T_{\rm eff}$ and gravity without having to resort to spectrum fitting. The synthetic spectrum calculation and our method of analysis are described in § 4. The results concerning several molecules of interest that are at least potentially detectable are presented in § 5, followed by a discussion in § 6. Finally, a summary of the results and directions for future study are given in § 7.

2. SPECTROSCOPIC OBSERVATIONS

Spectra of Gl 229B in selected narrow intervals in the *J*, *H*, and *K* windows were obtained at the 3.8 m United Kingdom Infrared Telescope (UKIRT) in 1998 January, using the facility spectrometer CGS 4 (Mountain et al. 1990) and its 150 l mm^{-1} grating. Details of the observations are provided in Table 1. These are among the highest resolution spectra obtained of any T dwarf.

The spectra were obtained in the standard stare/nod mode with the 1.″2 wide slit of the spectrometer oriented at a position angle of 45°, nearly perpendicular to the line connecting Gl 229A and Gl 229B. The southward-going diffraction spike of Gl 229A together with scattered light from that star, which is 10 mag brighter than Gl 229B, contaminated the array rows near and to the southwest of those containing the spectrum of Gl 229B. The contamination on the Gl 229B rows was determined by interpolation and was subtracted; typically it was comparable or somewhat smaller than the signal from Gl 229B. In order to remove telluric absorption features, spectra of the A0 V star BS 1849 were measured just prior to Gl 229B. In all cases the match in airmasses was better than 5%; hence, in the ratioed spectra residual telluric features are small compared to the noise level. Wavelength calibration was achieved by observations of arc lamps and is in all cases better than 1 part in 10^4 (2 σ).

The spectra shown in this paper have been slightly smoothed, so that the resolving powers are lower than those in Table 1 by approximately 25%. They also have been rebinned to facilitate co-adding like spectra and joining adjacent spectral regions. The error bars can be judged by the point-to-point variations in featureless portions of the spectra, and the signal-to-noise ratios at the continuum peaks are approximately 40 in the *K* band, 25 in the *H* band, and 30 in the *J* band. The flux calibration of each spectrum is approximate as no attempt was made to match the photometry of Gl 229B.

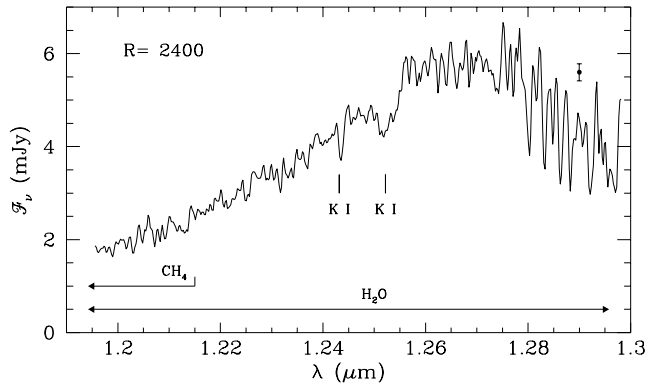

FIG. 1.—*J*-band spectrum. The spectral resolution is $R = 2400$, and the noise level at the maximum flux level is indicated by the error bar. Nearly all features in this spectrum are caused by H_2O absorption, except at short wavelengths where the CH_4 opacity becomes significant and for two strong K I lines. The flux calibration is approximate.

While we identify the spectra by their corresponding standard photometric infrared bandpass, their wavelength coverages are much narrower than the *JHK* filters and typically corresponds to the peak flux of Gl 229B in each bandpass.

In the *J*-band spectrum (Fig. 1), nearly all features are caused by H_2O. The short-wavelength end of the spectrum shows the red side of a CH_4 band, which is responsible for the features seen shortward of $\sim$1.215 μm. Two lines of neutral potassium are easily detected near 1.25 μm. No other lines of alkali metals fall within the wavelength coverage of our observations. The *H*-band spectrum (Fig. 2) is relatively rich in molecular opacity sources. All the features seen in the spectrum are either due to H_2O ($\lambda \lesssim 1.59$ μm) or part of a very strong CH_4 absorption band ($\lambda \gtrsim 1.6$ μm). Features seen between 1.59 and 1.6 μm cannot presently be ascribed with certainty and are due to either H_2O or CH_4. While the opacities of NH_3 and H_2S are not negligible in this part of the spectrum, neither molecule forms distinctive spectral features. Their presence cannot be directly ascertained from these data, mainly because their opacity is weaker than that of H_2O and CH_4 and because of significant pressure broadening (see § 5.3). The *K*-band flux emerges in an opacity window between a strong H_2O band and a strong CH_4 band (Fig. 3). Spectral features are caused by H_2O at shorter wavelengths ($\lambda \leq 2.11$ μm) and by CH_4 at longer wavelengths ($\lambda \geq 2.105$ μm). Several distinctive features of NH_3 are expected at the blue end of this spectrum and models predict a single absorption feature of H_2S at 2.1084 μm.

TABLE 1

OBSERVING LOG

UT DATE	WAVELENGTH (μm)	RESOLVING POWER	INTEGRATION TIME (minutes)	MEAN AIRMASS	
				Gl 229B	BS 1849
1998 Jan 25.....	2.10–2.18	3200	80	1.37	1.39
1998 Jan 25.....	2.02–2.10	3100	93	1.40	1.35
1998 Jan 26.....	1.53–1.61	2350	53	1.46	1.39
1998 Jan 26.....	1.25–1.30	3000	53	1.33	1.32
1998 Jan 26.....	1.20–1.25	2900	53	1.41	1.40
1998 Jan 27.....	2.02–2.10	3100	93	1.36	1.32

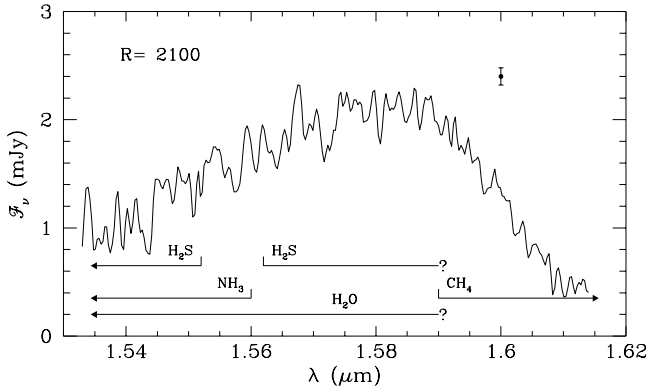

FIG. 2.—Same as Fig. 1 for the *H* band. The features seen in the spectrum are caused by H_2O for $\lambda \lesssim 1.59$ μm. At longer wavelengths, the rapid decrease in flux corresponds to the blue side of a strong CH_4 absorption band. Both NH_3 and H_2S have significant opacity in this spectral range but show no distinctive feature at this resolution. The flux calibration is approximate.

All features seen in Figures 1, 2, and 3 are unresolved blends of numerous molecular transitions. A spectral resolution at least 10 times higher would be required to resolve the intrinsic structure of the spectrum of Gl 229B.

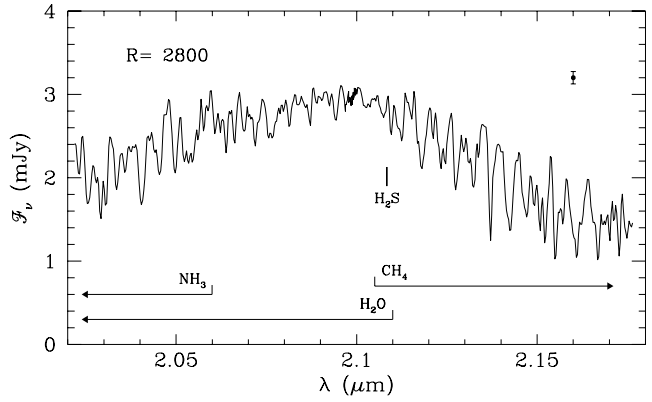

FIG. 3.—Same as Fig. 1 for the *K* band. The features seen in the spectrum are caused by H_2O for $\lambda < 2.11$ μm. At longer wavelengths, the rapid decrease in flux corresponds to the blue side of a strong CH_4 absorption band. Several strong NH_3 features are seen shortward of 2.06 μm. Models predict a single H_2S absorption feature at 2.1084 μm. The flux calibration is approximate.

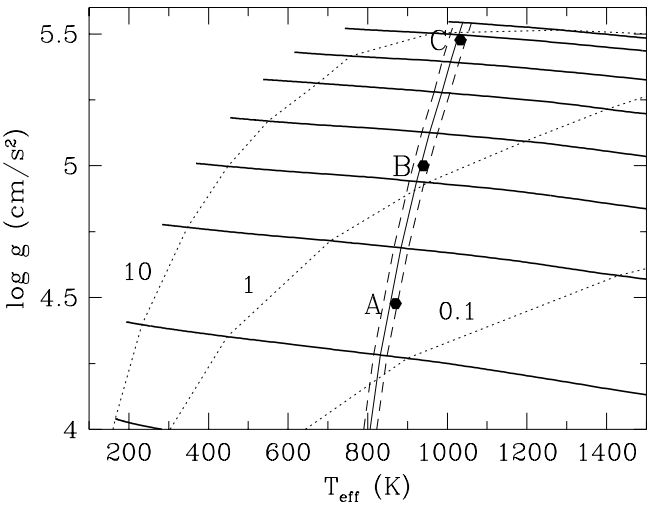

FIG. 4.—Evolution of solar metallicity brown dwarfs and giant planets in the effective temperature–gravity plane. The heavy solid lines are cooling tracks for objects with masses of 0.075, 0.07, 0.06, 0.05, 0.04, 0.03, 0.02, and 0.01 $M_\odot$, from top to bottom, respectively (Burrows et al. 1997). Evolution proceeds from right to left and isochrones (*dotted lines*) are labeled with the age in gigayears. The band crossing the center of the figure is the locus of all models with the luminosity of Gl 229 B ($L_{bol} = 6.2 \pm 0.55 \times 10^{-6}\ L_\odot$). Filled symbols correspond to the models listed in Table 2 and used for the present analysis.

3. EFFECTIVE TEMPERATURE AND GRAVITY

While synthetic spectra have been fairly successful at reproducing the unusual spectrum of Gl 229B (Marley et al. 1996; Allard et al. 1996; Tsuji et al. 1996), the entire spectral energy distribution has not yet been modeled satisfactorily. Limitations in the opacity databases are partly responsible for the remaining discrepancies between synthetic spectra and the data (see § 4.2). These shortcomings have impeded the determination of T_{eff} and of the gravity g in particular. On the other hand, the bolometric luminosity of Gl 229B is now well determined. Combining spectroscopic and photometric data from 0.82 to 10 μm with the parallax, Matthews et al. (1996) found $L = 6.4 \times 10^{-6}\ L_\odot$. With new *JHKL'* photometry, Leggett et al. (1999) found $L = 6.6 \pm 0.6 \times 10^{-6}\ L_\odot$. A recalibration using the *Hubble Space Telescope* (*HST*) photometry of Golimowski et al. (1998) gives $L = 6.2 \pm 0.55 \times 10^{-6}\ L_\odot$. Evolutionary models (Burrows et al. 1997) allow us to find a family of

TABLE 2

OPTIMAL PARAMETERS

MODEL	log *g* (cgs)	T_{eff} (K)	[*M*/H][a] 0.92 μm	*J*	*H*	*K*	$NH_3/(NH_3)_{eq}$ *H*[b]	*H*[c]	*K*
A	4.5	870	−0.5	−0.5	−0.3	−0.5	0	0.25	≲0.40
					−0.4		0.25	0.5	
					−0.5*		0.5	1	
B	5.0	940	−0.3	−0.2	−0.1	−0.3	0	≲0.25	≲0.40
					−0.2		0.25–0.5	0.5	
					−0.3*		>0.5	1	
C	5.5	1030	−0.2	0.1	0.0	−0.1	0.5	0.5	≲0.40
					−0.1*		1	1	

[a] Asterisk (*) indicates adopted metallicity.
[b] H_2S abundance set to 0.
[c] H_2S abundance from chemical equilibrium.

($T_{\rm eff}$, g) models with a given $L_{\rm bol}$. Figure 4 shows the cooling tracks of solar metallicity brown dwarfs in terms of the surface parameters $T_{\rm eff}$ and g. Models with the bolometric luminosity of Gl 229B fall within the band running through the center of the figure. Using a very conservative lower limit for the age of Gl 229A of 0.2 Gyr (Nakajima et al. 1995), we find $T_{\rm eff} = 950 \pm 80$ K. On the other hand, the gravity remains poorly determined with $\log g$ (cm s^{-2}) = 5 ± 0.5, corresponding to a mass range of 0.015–0.07 $M_\odot$. While the upper range is very close to the lower main-sequence mass limit, Gl 229B's status as a brown dwarf is secure. A star at the edge of the main sequence would be much hotter with $T_{\rm eff} \sim 1800$ K, well outside of Figure 4.

In the remainder of this paper, the discussion focuses on three atmosphere models that span the range of allowed solutions (Table 2 and Fig. 4): ($T_{\rm eff}$ (K), $\log g$ (cgs)) = (870, 4.5), (940, 5.0) and (1030, 5.5), which we label models A, B, and C, respectively. These constraints on $T_{\rm eff}$ and g from cooling sequences are quite firm. We find the same result, within the error bar on $L_{\rm bol}$, from several cooling sequences that predate Burrows et al. (1997). The latter were computed with different input physics such as the equation of state and surface boundary conditions derived from gray and nongray atmosphere models using several opacity tabulations.

In § 5, we show that these three models can fit the spectra only if they have different metallicities ranging from $[M/{\rm H}] = -0.1$ to -0.5. The evolution of brown dwarfs is sensitive to the metallicity through the atmospheric opacity, which controls the rate of cooling. We find that, for the range of interest here, the effect of a reduced metallicity on our determination of $T_{\rm eff}$, g, and the cooling age is smaller but comparable to that of the uncertainty on the value of $L_{\rm bol}$. We choose to ignore it for simplicity.

4. METHOD OF ANALYSIS

4.1. *Model Atmospheres and Spectra*

Our analysis is based on the atmosphere models of brown dwarfs and extrasolar giant planets described in Burrows et al. (1997). Briefly, the atmospheres are in radiative/convective equilibrium and the equation of radiative transfer is solved with the k-coefficient method. The chemical equilibrium is treated as in Burrows et al. (1997). Gas phase opacities include Rayleigh scattering, the collision-induced opacity of H_2, and the molecular opacities of H_2O, CH_4, NH_3, H_2S, PH_3, and CO, as well as the continuum opacities of H^- and H_2^-. The molecular line opacity database is described in more detail in § 4.2. Atomic line opacity is not included. Because of the relatively large gravity of Gl 229B, pressure broadening of the molecular lines plays an important role in determining the (T, P) profile of the atmosphere and in shaping the spectrum. The line-by-line broadening theory we use is described in Burrows et al. (1997). The strong continuum opacity source responsible for the rapid decrease of the flux of Gl 229B shortward of 1.1 μm is included following the haze model of Griffith et al. (1998). Details of the haze model and of our fitting procedure are given in § 5.1. The (T, P) structures of these atmosphere models are shown in Figure 5. The profiles intersect each other because both $T_{\rm eff}$ and the gravity vary between the models. The inflexion point at $\log T \sim 3.25$ signals the top of the convection zone.

Using the same monochromatic opacities used to compute the k-coefficients, high-resolution synthetic spectra are generated from the atmospheric structures by solving the radiative transfer equation with the Feautrier method on a frequency grid with $\Delta\nu = 0.1$ cm^{-1}. Spectra with resolution lower than $\Delta\nu \gtrsim 1$ cm^{-1} can then be generated for comparison with data.

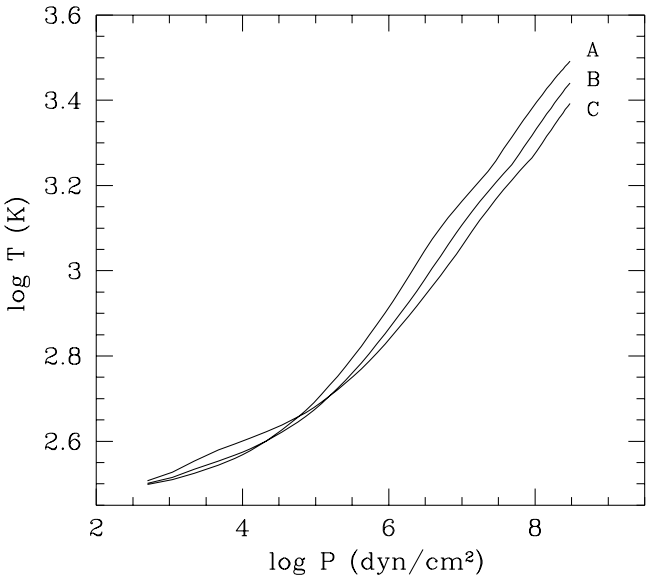

FIG. 5.—Temperature-pressure profiles of the three atmosphere models used in this analysis. Labels correspond to the models shown in Fig. 4 and Table 2.

An unusual aspect of T dwarf atmospheres is the great variation of the opacity with wavelength. These atmospheres are strongly nongray and the near-infrared spectrum is sculpted by strong absorption bands of H_2O and CH_4. Most of the flux emerges in a small number of relatively transparent opacity windows. The concept of photosphere becomes rather useless since the level at which the spectrum is formed depends strongly on the wavelength. Figure 6 shows the depth of the "photosphere" ($\tau_\nu = \frac{2}{3}$) in both temperature and pressure as a function of wavelength for model B ($T_{\rm eff} = 940$ K, $\log g = 5$). In the Z, J, and H bands, and, to a lesser extent, in the K and M bands, the atmosphere is very transparent and can be probed to great depths. For $\lambda \gtrsim 25$ μm, the spectral energy distribution approaches a Planck function with $T \sim 500$ K.

Figure 6 reveals that spectroscopy between 0.8 and 12 μm can probe the atmosphere from $T \sim 500$ K down to a depth where $T \sim 1600$ K, corresponding to a range of 6 pressure scale heights! This provides an exceptional opportunity to study the physics of the atmosphere of a brown dwarf over an extended vertical range. The top of the convection zone for model B (located at $T = 1860$ K) is below the "photosphere" at all wavelengths and is not directly observable, however.

4.2. *Limitations to This Study*

Given the range of acceptable values of $T_{\rm eff}$ and g (§ 3), we can determine the metallicity of Gl 229B and the abundance of several key molecules by fitting synthetic spectra to the observations, for each of the three models. The precision of our results is determined by the reliability of the models, by the noise level in the data and, most significantly, by the

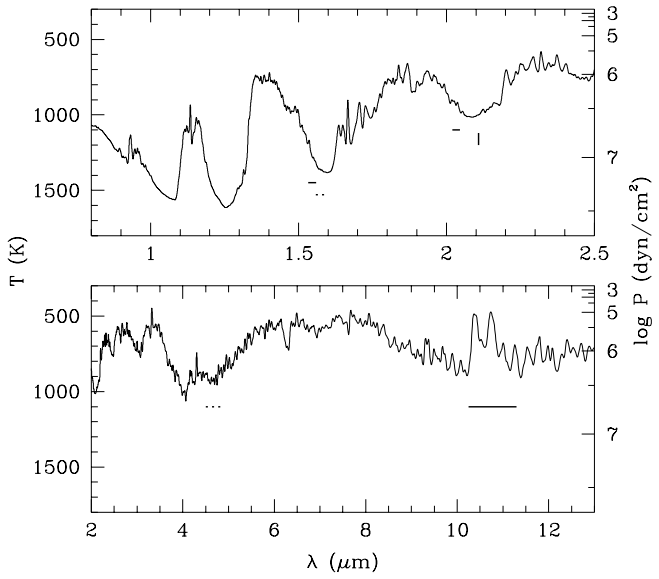

FIG. 6.—Temperature and pressure at the photosphere ($\tau_\lambda = \frac{2}{3}$) as a function of wavelength for model B ($T_{\rm eff} = 940$ K, $\log g = 5$). The temperature plotted (*left axis*) is equivalent to a brightness temperature. Horizontal bars indicate the wavelength range of NH_3 (*solid lines*) and CO (*dotted lines*) bands. The short vertical bar indicates a H_2S absorption feature at 2.1084 μm (see § 5.4.2).

limitations of the molecular line lists used to compute their opacities. The latter point requires a detailed discussion.

The opacities of CH_4 and NH_3 are computed from line lists obtained by combining the HITRAN (Rothman et al. 1998) and GEISA (Husson et al. 1992) databases, which are complemented with recent laboratory measurements and theoretical calculations. Further details are provided in Burrows et al. (1997). The resulting line lists for these two molecules are very nearly complete for $T < 300$ K, and their degree of completeness decreases rapidly at higher temperatures, where absorption from excited levels becomes important. Furthermore, the line list of CH_4 is limited to $\lambda > 1.584$ μm. We extend the CH_4 opacity to shorter wavelengths with the laboratory measurements of Strong et al. (1993), which provide the absorption coefficient averaged over intervals of 5 cm^{-1} between 1 and 5 μm at $T = 300$ K. We use Strong et al. (1993) opacities for $1 < \lambda < 1.82$ μm and the line list for $\lambda > 1.82$ μm. This puts the transition from one tabulation to the other in a strong H_2O absorption band and obliterates any discontinuity in CH_4 opacity at the transition. For $\lambda < 1$ μm, the tabulation of Karkoschka (1994) gives the absorption coefficient of CH_4 determined from spectroscopic observations of the giant planets at 0.0004 μm intervals. Because of the low temperatures found in the atmospheres of giant planets, the Karkoschka CH_4 opacities are appropriate for $T \lesssim 200$ K. To our knowledge, this compilation of NH_3 and CH_4 opacity is the most complete presently available.

As can be seen in Figure 5, the temperature in the atmosphere of Gl 229B is everywhere greater than 300 K. For CH_4, we compute temperature-dependent line opacity (which is incomplete above 300 K) from the population of excited levels determined by the Boltzmann formula for $\lambda > 1.82$ μm, and use temperature independent opacity at shorter wavelengths. While the synthetic spectra computed reproduce the fundamental band of CH_4 very well (centered at $\lambda = 3.4$ μm), the match with the 1.6 and 2.3 μm bands is rather poor. Even though CH_4 is a very prominent molecule in the spectrum of Gl 229B, the current knowledge of its opacity is not adequate for a quantitative analysis of its spectral signature. For this reason, we have essentially ignored the regions in our spectra where CH_4 is prominent. Unfortunately, this prevents us from estimating the abundance of CH_4—and therefore of carbon—in Gl 229B.

Ammonia shows significant absorption in both the *H*- and *K*-band spectra. The line list for NH_3 starts at $\lambda > 1.415$ μm. Because the line list does not include transitions from highly excited levels that occur at $T > 300$ K, the NH_3 opacity we compute at a given wavelength is strictly a lower limit to the actual opacity.

Except for the collision-induced absorption by H_2, the most important molecular absorber in Gl 229B is H_2O, for which the opacity is now relatively well understood. We use the most recent and most extensive ab initio line list (Partridge & Schwenke (1997), 3×10^8 transitions). This line list is essentially complete for $T \lesssim 3000$ K. As a demonstration of the quality of this database, we find that the H_2O features computed with this line list correspond extremely well in frequency with the observed features of Gl 229B (e.g., Figs. 7, 8, and 9). However, we find noticeable discrepancies in the relative strengths of H_2O features, which we attribute to the calculated oscillator strength of the transitions (§ 5.1). This effect can also be seen in Figure 1*c* of Griffith et al. (1998). At high resolution, the distribution of molecular transitions in frequency and strength is nearly random, and the inaccuracies in oscillator strengths we have found limit the accuracy of model fitting in a fashion similar to noise. This "opacity noise" is at least as significant as the noise intrinsic to our data.

5. RESULTS FROM FITTING THE SPECTRA

We have constructed a grid of synthetic spectra for the three models shown in Figure 4 with metallicity $-0.7 \leq$ [M/H] ≤ 0.1 in steps of 0.1. We use these modeled spectra to fit four distinct spectral regions (the "red," *J*, *H*, and *K* spectra) separately to determine the metallicity as a function of gravity with an internal precision of ± 0.1 dex. For the purpose of fitting the data, the synthetic spectra were renormalized to the observed flux at a selected wavelength in each spectral region.

The model spectra show some distortions in the overall shape of the spectrum, which are probably due to remaining uncertainties in the (*P*, *T*) profile of the atmosphere, the inadequate CH_4 opacities, and possible effects of dust opacity. Considering the additional problems with the strength of the H_2O features, we elected to do all fits by eye, except where otherwise noted. We discuss the fitting of each spectral interval below. In the interest of brevity, we present a detailed discussion of fits obtained only with the model of intermediate gravity (model B). The best fits obtained with models A and C are very nearly identical to those with model B. The results are summarized in Table 2.

5.1. *The "Red" Spectrum*

The "red" spectrum extends from 0.83 to ~ 1 μm and is formed deep in the atmosphere where $1100 < T < 1500$ K. The spectra of Schultz et al. (1998) and Oppenheimer et al. (1998) reveal two lines of Cs I (at 0.852 and 0.894 μm) and a strong H_2O band but *not* the bands of TiO and VO common to late M dwarfs and early L dwarfs (Fig. 7). Ref-

ractory elements, such as Ti, Fe, V, Ca, and Cr, are expected to be bound in condensed compounds in a low-temperature atmosphere such as that of Gl 229B and therefore are not available to form molecular bands (Fegley & Lodders 1996; Marley et al. 1996; Burrows & Sharp 1999). With the exception of the strong, unidentified feature at 0.9874 μm, all features between 0.89 and 1.0 μm can be attributed to H_2O. An overlap of a weak band of H_2O and a weaker CH_4 band causes the small depression at 0.894 μm, which was tentatively attributed to CH_4 by Oppenheimer et al. (1998) and Schultz et al. (1998). Features below 0.89 μm cannot be identified at present. The two Cs I lines are not included in our model.

The flux from Gl 229B is also observed to decrease very rapidly toward shorter wavelengths (Schultz et al. 1998; Oppenheimer et al. 1998; Golimowski et al. 1998), which, in the absence of the strong TiO and VO bands, is evidently caused by the presence of a missing source of opacity in the atmosphere. Spectra computed with molecular opacities only (but excluding TiO, VO, FeH, etc.) predict visible fluxes that are grossly overestimated (Griffith et al. 1998) but the detailed sequence of absorption features of the spectrum are well reproduced, indicating that the short-wavelength flux is suppressed by a *smooth* opacity source.

We fit the red spectrum of Gl 229B between 0.82 and 1.15 μm to obtain the metallicity. We have recalibrated the published spectrum (Oppenheimer et al. 1998; Geballe et al. 1996; Leggett et al. 1999) using the *HST* photometry of Golimowski et al. (1998). We model the continuum opacity with a layer of condensates following the approach of Griffith et al. (1998). Condensates are expected in the atmosphere of Gl 229B on the basis of chemical equilibrium calculations (Lodders 1999; Burrows & Sharp 1999) and can provide the required opacity. Alternatively, Tsuji et al. (1999) and Burrows et al. (2000b) attribute this rapid decline to the pressure broadened red wing of the 0.77 μm K I resonance doublet. The first optical spectrum of a T dwarf (SDSS 1624+0029) shows that the latter explanation is correct (Liebert et al. 2000). The nature of this opacity source is not very important for the determination of the metallicity, however, as long as the proper continuum opacity background is present in the calculation.

The dust opacity is computed with the Mie theory of scattering by spherical particles (Bohren & Huffman 1983) and is determined by the vertical distribution of the particles, their grain size distribution, and the complex index of refraction of the condensate. The cloud model of Griffith et al. (1998) is described by (1) the vertical density profile of the condensate, taken as

$$n_d = AP \ ,$$

where n_d is the number density of condensed particles, P is the ambient gas pressure, and the cloud layer is bound by

$$P_{\rm top} \leq P \leq 100 \text{ bar} \ ;$$

(2) the size distribution of the particles

$$f(d) = \frac{d}{d_0} \exp\left[\frac{\ln\ (d/d_0)}{\ln\ \sigma}\right]^2 \ ,$$

where d is the diameter of the particles; and (3) the complex index of refraction of the condensate

$$n(\lambda) = 1.65 + in_i(\lambda) \ ,$$

where $P_{\rm top}$, A, d_0, σ, the function $n_i(\lambda)$, and the metallicity of the atmosphere are free parameters.

Such a multiparameter fit of the observed spectrum is not unique. Furthermore, arbitrarily good fits of the "continuum" flux level can be obtained by adjusting the imaginary part of the index of refraction since its wavelength dependence is weakly constrained a priori. Our results for the three models are qualitatively similar to those of Griffith et al. (1998). Typical values of the fitted dust parameters are $A = 415$ cm^{-3} bar^{-1}, $P_{\rm top} = 0.5$ bar, $d_0 = 0.21$ μm, and $\sigma = 1.3$, with the imaginary part of the index of refraction decreasing from $n_i = 1.70$ at 0.8 μm to 0.01 at 1.10 μm. These parameters applied to model B with a metallicity of $[M/\mathrm{H}] = -0.3$ result in the fit shown in Figure 7.

The metallicity of the atmosphere $[M/\mathrm{H}]$ is largely independent of the dust parameters, however, as it is constrained by the amplitude of the features in the H_2O band that we fit between 0.925 and 0.98 μm. A larger metallicity results in a larger amplitude of the features inside the band. We obtain the same value of $[M/\mathrm{H}]$ as long as a good fit of the "continuum" flux level is obtained, regardless of the particular values of dust parameters. The lower panel of Figure 7 clearly shows differences in the relative strengths of the absorption features in the H_2O band between the synthetic and observed spectra. Similar differences also occur in the J, H, and K bands. The same differences are found for all three atmospheric profiles and point to inaccuracies in the oscillator strength of the ab initio line list of H_2O (Partridge & Schwenke 1997). The metallicity is fitted to give the best overall fit of these features with a precision of ± 0.1 dex.

Strictly speaking, this procedure gives the H_2O abundance, or $[\mathrm{O/H}]$ rather than $[M/\mathrm{H}]$. For solar metallicity, the condensation of silicates deep in the atmosphere of Gl 229B will reduce the amount of oxygen available to form H_2O by $\sim 15\%$ (Fegley & Prinn 1988), which implies that

$$[M/\mathrm{H}] = [\mathrm{O/H}] + 0.07 \ . \quad (1)$$

The correction, which decreases for subsolar metallicities, is smaller than our fitting uncertainty and will be ignored hereafter.

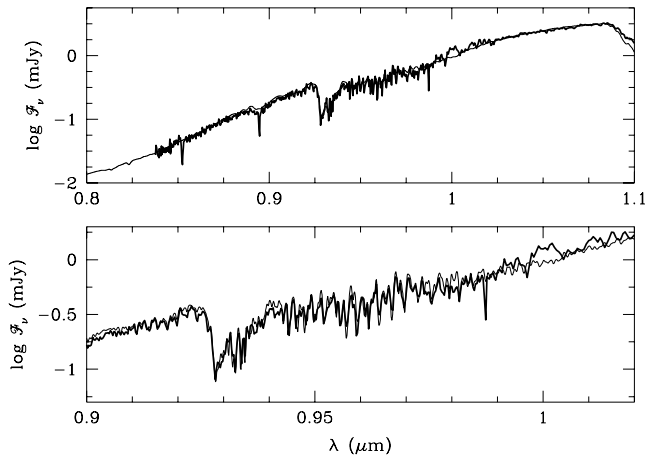

FIG. 7.—Spectrum computed with model B, $[M/\mathrm{H}] = -0.3$, and dust opacity (*thin line*) compared to the observed spectrum of Oppenheimer et al. (1998; *heavy line*). *Top panel*: Entire fitted region. *Bottom panel*: Details of the H_2O absorption band at a resolution $R = 2250$.

5.2. *J-Band Spectrum*

The *J*-band spectrum probes the most transparent window of the spectrum of Gl 229B and is formed at great depth where 1500 K $\leq T \leq$ 1600 K and $P \sim 30$ bar (Fig. 6). Our spectrum contains almost exclusively H_2O features, with the exception of CH_4 absorption for $\lambda \lesssim 1.215$ μm and of two prominent K I lines (Fig. 1). Since we have elected to ignore CH_4 bands and our synthetic spectra do not include alkali metal lines, we fit the *J* spectrum between 1.215 and 1.298 μm to determine the metallicity from the depth of the H_2O absorption features. Figure 8 shows the effect of the metallicity on the spectrum (*top panel*) and our best fit (*bottom panel*) for model B. The flux level in the *J* spectrum varies by a factor of 3, and our best fit shows distortions in the general shape of the spectrum. The distortions may be caused by a combination of uncertainties in the (T, P) profile of the atmosphere, problems with the H_2O opacities or a small amount of dust opacity in the infrared spectrum of Gl 229B (not modeled). Since the fit is based on the depth of the features, we ignore these distortions and fit the logarithm of the flux rather than the flux, as shown in Figure 8. As in the red spectrum (§ 5.1), we find a remarkable correspondence of spectral features between the observed and modeled spectra although the model spectrum is somewhat less successful at reproducing the relative strengths of the H_2O features.

5.3. *H-Band Spectrum*

While the *H*-band spectrum falls between the red side of a strong H_2O band (for $\lambda \lesssim 1.59$ μm) and the blue side of a prominent CH_4 band (for $\lambda \gtrsim 1.59$ μm), NH_3 and H_2S have nonnegligible opacity in this wavelength interval, which also includes a band of CO.

The strong CH_4 band is responsible for the turnover of the flux at 1.59 μm. In this wavelength range, the CH_4 opacity is described in our calculation by the Strong et al. (1993) laboratory measurements, which are restricted to $T = 300$ K. As a consequence, the CH_4 band comes in at 1.61 μm in the synthetic spectra, which results in strong departures of the mean flux level between data and models for $\lambda > 1.58$ μm. This limits our analysis of the *H*-band spectrum to wavelengths shorter than 1.58 μm. In this wavelength range, the spectrum is formed deep in the atmosphere, where 1200 < T < 1350 K and $P \sim 10$ bar (Fig. 6). Within this spectral region, we determine the abundance of NH_3 as a function of the metallicity but cannot untangle the two. We also comment on the presence of H_2S and CO.

5.3.1. *Metallicity and Ammonia*

While NH_3 absorption can significantly affect the slope of the spectrum shortward of 1.56 μm (Fig. 9), there is no distinctive feature at this spectral resolution ($R = 2100$) to provide an unambiguous detection of this molecule. The detection of CO at 4.7 μm well above the equilibrium abundance (Noll et al. 1997) suggests the possibility that NH_3 may also depart from its chemical equilibrium abundance (Fegley & Lodders 1994). We therefore vary the abundance of NH_3 by reducing its chemical equilibrium abundance—*as computed for a given metallicity*—uniformly throughout the atmosphere by constant factor. We found that reduction factors of 1, 0.5, 0.25, and 0 provide an adequate grid of NH_3 abundances given the signal-to-noise ratio (S/N) of the data and the residual problems with the H_2O opacity.

The effect of varying the metallicity on the *H*-band spectrum is shown in Figure 10 for model B. All spectra in Figure 10 were computed with the equilibrium abundance of NH_3. In this case, we find a best-fitting metallicity of $[M/H] = -0.3$. Figures 9 and 10 show that varying the abundance of NH_3 and varying the metallicity have very similar effects on the synthetic spectrum. In the absence of any distinctive feature of NH_3, it is not possible to determine both the metallicity and the NH_3 abundance separately. For each value of $[M/H]$, we can adjust the NH_3 abundance to obtain a good fit, with higher metallicities requiring lower NH_3 abundances. The best-fitting solutions are given in Table 2. These fits are nearly indistinguishable from each other, although the higher metallicity fits are marginally better.

It is in the *H* band that we find the poorest match in the detailed features of the data and the models. While the fit is

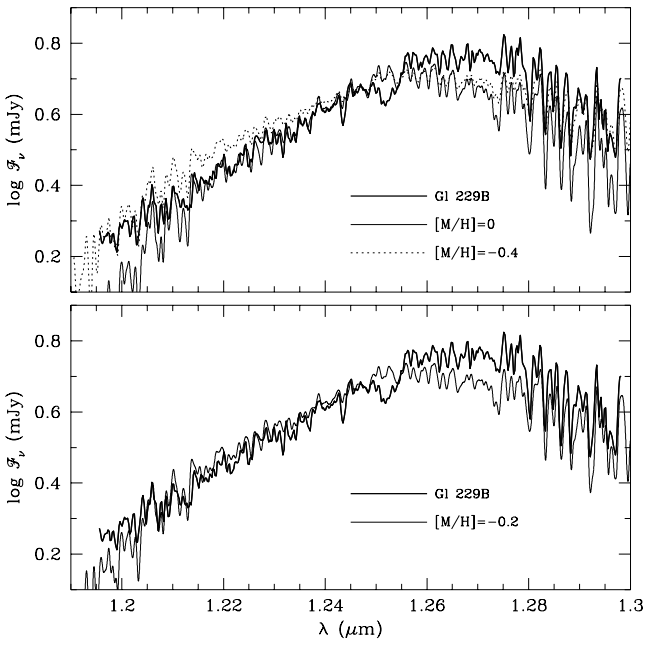

FIG. 8.—*Top panel*: Effect of the metallicity on the *J*-band spectrum. Data are compared to two model B spectra with $[M/H] = -0.4$ and 0. *Bottom panel*: Best fit for model B is obtained for $[M/H] = -0.2$. See text. The synthetic spectra are normalized to the observations at 1.2472 μm and are plotted at the same resolution ($R = 2400$).

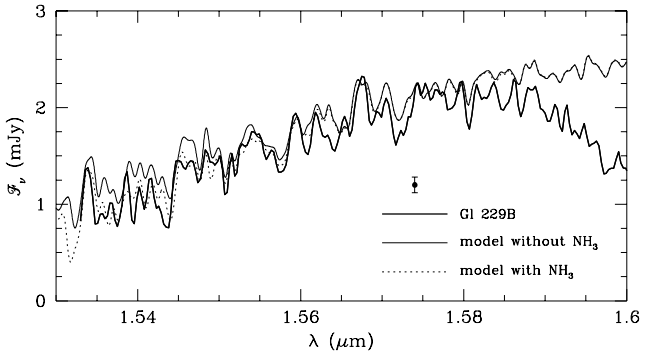

FIG. 9.—Effect of the NH_3 abundance on the *H*-band spectrum. The spectrum is computed for model B with $[M/H] = -0.3$ with the chemical equilibrium abundance of NH_3 (*dotted line*) and without NH_3 opacity (*solid line*). The dotted curve represents our best fit for this value of $[M/H]$. The synthetic spectra are normalized to the observations at 1.5744 μm and plotted at the same resolution ($R = 2100$).

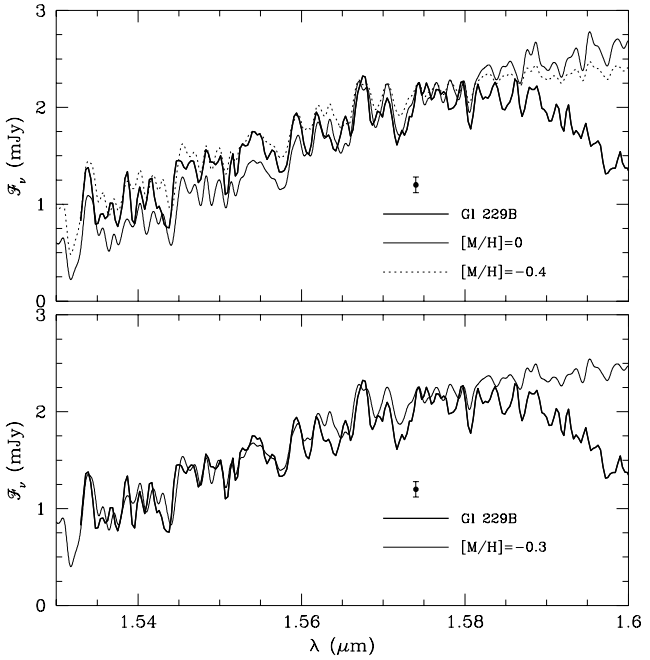

FIG. 10.—*Top panel*: Effect of the metallicity on the *H*-band spectrum. Data are compared to two model B spectra with $[M/H] = -0.4$ and 0. *Bottom panel*: The best fit for model B is obtained for $[M/H] = -0.3$. In all cases, the NH_3 abundance is determined from the chemical equilibrium. See text. See Fig. 9 legend for additional details.

determined by matching the relative amplitudes of the features, the two-parameter fit (metallicity and NH_3 abundance) we have performed amounts to little more than fitting the slope of the spectrum. As an internal check on our fitting procedure and precision, we have verified that our fits indeed have the same slope as the data by plotting data and models at a very low spectral resolution, which eliminates all absorption features.

5.3.2. *Hydrogen Sulfide*

Hydrogen sulfide (H_2S) has nonnegligible opacity over most of the wavelength range of our fit to the *H* band. Figure 11 shows two spectra computed with and without H_2S opacity. Its opacity is weaker than that of NH_3 however, and there are no distinctive features that would allow a positive identification. Since the H_2S features are fairly uniformly distributed in strength and wavelength, fitting the spectrum with either the chemical equilibrium abundance of H_2S or with no H_2S at all has only a small-to-negligible effect on the determination of the NH_3 abundance for a given metallicity (Table 2). For the low-gravity model A, the NH_3 abundance determined from spectra without H_2S is about one-half of the value found with the chemical equilibrium abundance of H_2S. The difference decreases at higher gravities and is negligible for model C.

Chemical equilibrium calculations (Fegley & Lodders 1996; Lodders 1999) indicate that H_2S is present in Gl 229B with an abundance essentially equal to the elemental abundance of sulfur in the atmosphere (see § 6.3 for further discussion). Unfortunately, we are unable to ascertain the presence of H_2S in the atmosphere of Gl 229B at present.

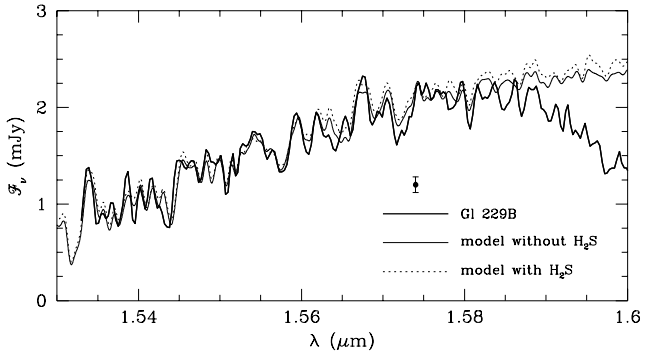

FIG. 11.—Effect of the H_2S abundance on the *H*-band spectrum. The spectra are computed for model B with $[M/H] = -0.3$ with the chemical equilibrium abundance of H_2S and without H_2S opacity. See Fig. 9 legend for additional details.

5.3.3. *Carbon Monoxide*

The discovery of CO in the 4.7 μm spectrum of Gl 229B with an abundance about 3 orders of magnitude higher than predicted by chemical equilibrium revealed the importance of dynamical processes in its atmosphere (Fegley & Lodders 1996; Noll et al. 1997; Griffith & Yelle 1999). The 4.7 μm spectrum probes the atmosphere at the 2–3 bar level, where $T \sim 900$ K (Fig. 6). At this level, chemical equilibrium calculations predict a CO abundance of $X_{CO} = 4.7 \times 10^{-8}$, while Noll et al. (1997) found $5 \times 10^{-5} \lesssim X_{CO} \lesssim 2 \times 10^{-4}$. The second overtone band of CO falls within the *H* band and, in principle, could provide a determination of X_{CO} at a deeper level of the atmosphere where $P \sim 14$ bar and $T \sim 1400$ K (Fig. 6). Figure 12 shows a comparison of the data with synthetic spectra computed with various amounts of CO for model B with solar metallicity. The first two spectra are computed with the chemical equilibrium abundance of CO ($X_{CO} = 4.90 \times 10^{-5}$ at 14 bar) and without CO ($X_{CO} = 0$). These two spectra are very nearly identical. A third spectrum is computed in the unrealistic limit where all the carbon in the atmosphere is in the form of CO ($X_{CO} = 2.97 \times 10^{-4}$), which represents the maximum possible CO enhancement. As we found for NH_3 and H_2S, there is no distinctive spectral signature of CO at this resolution ($R = 2100$). Our extreme case represents a flux reduction of $\sim 2\,\sigma$ at best. We are unable to constrain the CO abundance with our data. Since the $\Delta v = 3$ band of CO is $\sim 10^3$ times weaker than the fundamental band at 4.7 μm, obtaining a useful CO abundance from *H*-band spectroscopy will be a difficult undertaking.

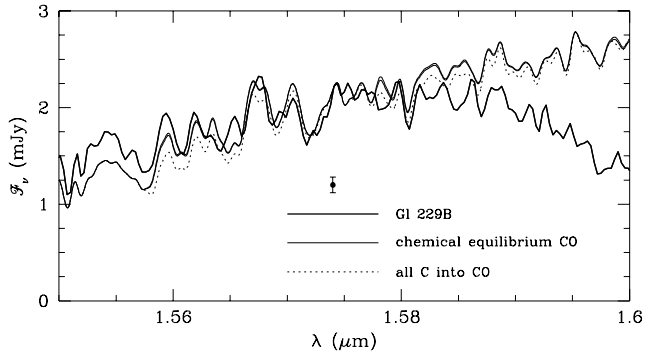

FIG. 12.—Carbon monoxide absorption band in the *H* band. The spectra are computed for model B with $[M/H] = 0$ with the chemical equilibrium abundance of CO (*solid line*) and with the CO abundance equal to the elemental carbon abundance (*dotted line*). A spectrum computed with the CO abundance set to zero overlaps the equilibrium CO curve. See Fig. 9 legend for additional details.

5.4. *K-Band Spectrum*

Of our three near-infrared spectra, the *K*-band spectrum is formed highest in the atmosphere: $T = 950$–1020 K and $P \sim 3$ bar (Fig. 6). This is the same level as is probed with 4.7 μm spectroscopy. As in the *H* band, the spectrum contains mainly H_2O features on the blue side ($\lambda \lesssim 2.1$ μm) and a strong CH_4 band appears at longer wavelengths. There are also several NH_3 features for $\lambda < 2.05$ μm, and the models predict an isolated feature of H_2S (Fig. 3).

Figure 13 compares a spectrum computed for model B with $[M/H] = -0.3$ with the entire *K*-band spectrum. There is an excellent agreement in the structure of the spectrum even though the overall shape is not very well reproduced. For $\lambda < 2.05$ μm, the model predicts strong features of NH_3, which we discuss in the next section. Beyond 2.12 μm is a CH_4 band, which is too weak in the model. The structure within the modeled band is remarkably similar to the observed spectrum, however. This much better agreement of the CH_4 band than we obtained in the *H* band is due to two factors. First, in this band the CH_4 opacity is computed from a line list and can therefore be computed as a function of temperature rather than at a fixed value of 300 K. Second, the lower temperature where the band is formed (Fig. 6) reduces the effect of the incompleteness of the CH_4 line list above 300 K. Nevertheless, we do not consider the CH_4 features here and limit our analysis to $\lambda \leq 2.10$ μm.

The *K*-band spectrum provides a unique opportunity: once the metallicity is determined by matching the depth of the H_2O features between 2.05 and 2.10 μm, the abundance of NH_3 can be obtained by fitting its features below 2.05 μm. The fit of the metallicity is shown in Figure 14 for model B, which shows $[M/H] = 0$ and -0.5 (*top panel*) and our best fit, $[M/H] = -0.3$ (*bottom panel*). Values for models A and C are given in Table 2. All features in this region are due to H_2O, and, as we found in the red spectrum and in the *J* and *H* bands, the oscillator strengths of the H_2O line list do not reproduce the relative strength of the observed features very well.

5.4.1. *Ammonia*

In the wavelength range shown in Figure 15, the spectrum consists of a few NH_3 features on a background of H_2O absorption. Synthetic spectra predict seven strong NH_3 features in this spectrum, of which three (2.033, 2.037, and 2.046 μm) are clearly present, one (2.041 μm) is absent, and three (2.026, 2.029, and 2.031 μm) appear to be missing. This constitutes an ambiguous detection of NH_3 in Gl 229B. The determination of the abundance of NH_3 from the *K*-band spectrum is hampered by the limited accuracy of the oscillator strengths of the H_2O line list and by the incompleteness of our NH_3 line list for temperatures above

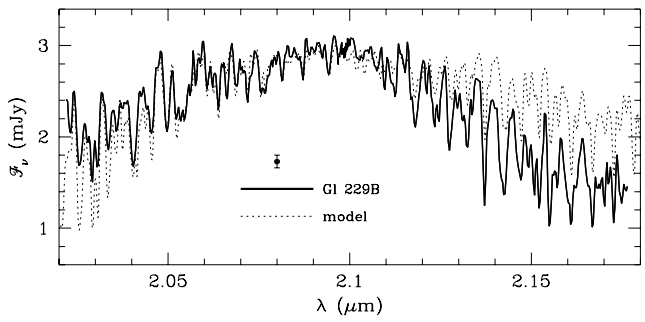

FIG. 13.—Synthetic spectrum for model B with $[M/H] = -0.3$ compared to the observed *K*-band spectrum. The synthetic spectrum is normalized to the data at 2.0513 μm and plotted at the same resolution ($R = 2800$).

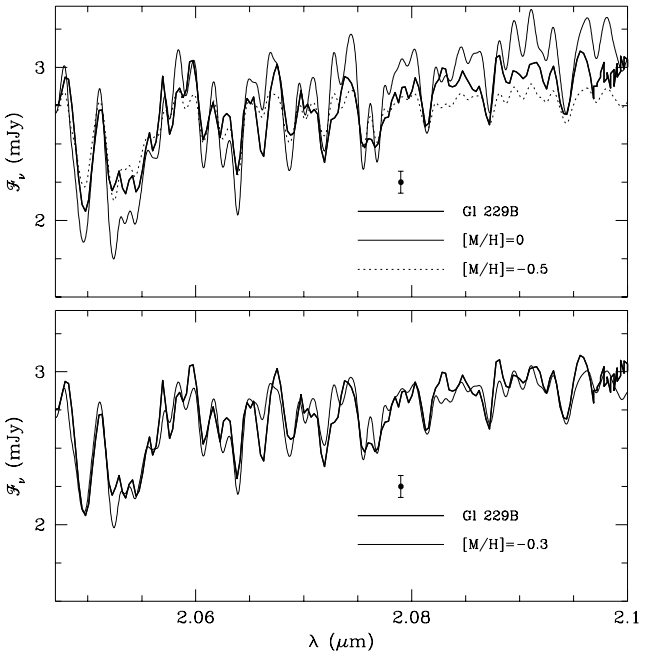

FIG. 14.—*Top panel*: Effect of the metallicity on the *K*-band spectrum. Data are compared to two model B spectra with $[M/H] = -0.5$ and 0. *Bottom panel*: The best fit for model B is obtained for $[M/H] = -0.3$. All features in this figure are caused by H_2O. See Fig. 13 legend for additional details.

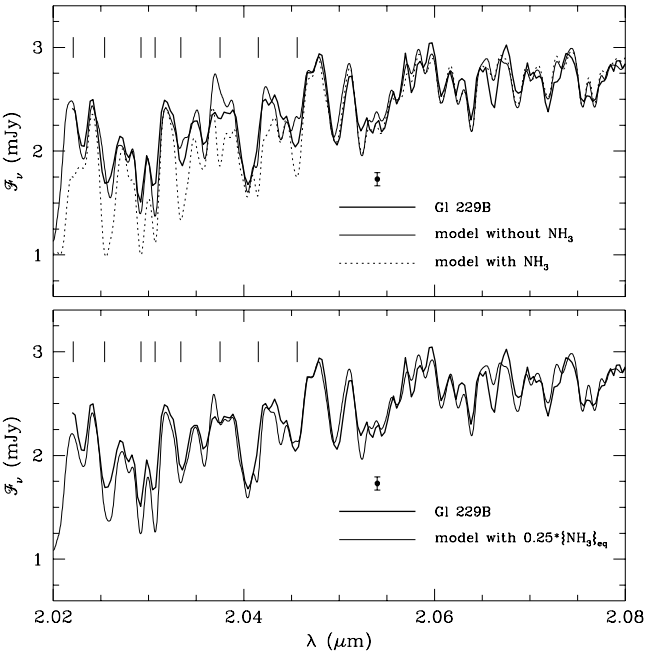

FIG. 15.—Portion of the *K*-band spectrum, which shows NH_3 features. The data are shown by the heavy solid line, with a representative error bar. Ammonia features are indicated by tick marks. *Top panel*: Synthetic spectrum computed from model B with $[M/H] = -0.3$ (*dotted line*) and after removing all NH_3 opacity (*thin solid line*). *Bottom panel*: Same as above but the equilibrium NH_3 abundance has been uniformly reduced by a factor of 0.25 throughout the atmosphere. See Fig. 13 legend for additional details.

300 K. The effect of the former can be seen in the trio of features at 2.026, 2.029 and 2.031 μm, which overlap H_2O absorption features. Even after removing all NH_3 opacity, these features are still too strong in the calculated spectrum (*top panel* of Fig. 15). The top panel of Figure 15 as well as Figure 13 show that for model B, the abundance of NH_3 derived from the chemical equilibrium for the adopted metallicity of $[M/H] = -0.3$ is too high. We therefore consider a depletion in NH_3 in the atmosphere of Gl 229B at the level probed by the *K*-band spectrum. Following the approach used in fitting the *H*-band spectrum, we express this depletion as a fraction of the chemical equilibrium abundance of NH_3 for the metallicity obtained independently from the amplitude of the H_2O features in the *K* band. This fraction is applied uniformly throughout the atmosphere for the computation of the synthetic spectrum. Given the ambiguous presence of NH_3 in the *K* band, we have determined the optimal NH_3 abundance by minimizing the χ^2 of the spectral fit for $2.022 \leq \lambda \leq 2.049$ μm. This gives a depletion factor of $\lesssim 0.4$ with no NH_3 present being an acceptable fit. Restricting the fit to the region where NH_3 features are clearly observed ($2.032 \leq \lambda \leq 2.049$) gives a similar result but favors a finite value for the NH_3 depletion of ~ 0.2. The results are summarized in Table 2. The lower panel of Figure 15 shows the model B fit obtained by reducing the NH_3 abundance throughout the atmosphere to $\sim 25\%$ of its chemical equilibrium value *for the adopted metallicity*. With this significant degree of depletion, the model reproduces the three detected features (2.033, 2.037, and 2.046 μm) extremely well and makes the 2.041 μm feature consistent with the observations.

Because our NH_3 line list is incomplete at high temperatures, the opacity that we compute is strictly a lower limit to the actual NH_3 opacity at any wavelength. If the incompleteness is significant for the features found in the *K*-band spectrum, then the NH_3 abundance is actually lower still. It appears extremely unlikely that the errors in the oscillator strength of the H_2O transitions would conspire to mimic the depletion of NH_3 that we find. For example, if we imagine that there is no NH_3 depletion (*dotted curve* in the *top panel* of Fig. 14), the residuals between the data and the fitted spectrum for $\lambda < 2.05$ μm would be much larger than the typical mismatch that we find in H_2O features in all four spectra presented here. We consider the depletion of NH_3 in the *K*-band spectrum to be firmly established.

5.4.2. *Hydrogen Sulfide*

We are not able to establish the presence of H_2S from our *H*-band spectrum (§ 5.3.2). Throughout the *K* band, the H_2S opacity is generally overwhelmed by H_2O and CH_4 absorption. However, there is a peak in the opacity of H_2S that is about 1 order of magnitude higher than all other opacity maxima (Fig. 16). Our synthetic spectra indicate that this feature is strong enough to become visible in the midst of the background of H_2O and CH_4 features. Figure 17 shows the relevant portion of the *K*-band spectrum with synthetic spectra for all three models (A, B, and C) using the fitted metallicity (Table 2). All three panels are remarkably similar. The strength of the predicted feature is well above the noise level of the data, and taken at face value Figure 17 indicates a probable depletion of H_2S by more than a factor of 2. On the other hand, chemical equilibrium calculations

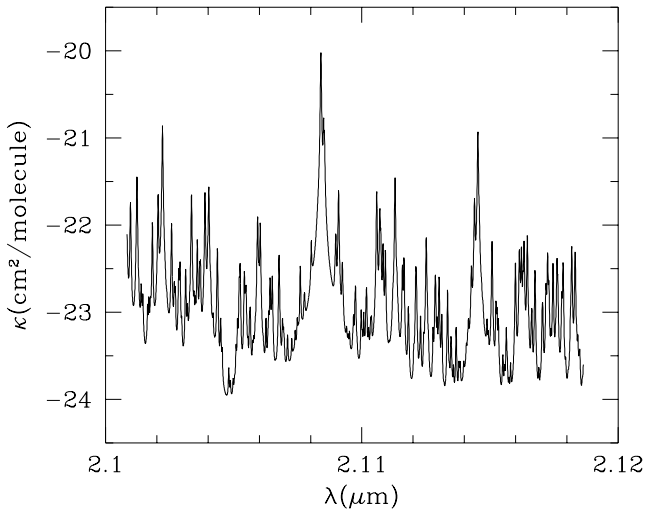

FIG. 16.—Opacity of H_2S in the 2.11 μm region for $T = 800$ K and $P = 1$ bar. The spectral resolution is $R = 4.8 \times 10^5$. Synthetic spectra predict that the strong feature at 2.1084 μm should be observable.

indicate that the H_2S abundance should be very near the elemental abundance of sulfur, even in the presence of vertical transport and condensation (Fegley & Lodders 1996). Since there is no reason to expect a significant depletion of H_2S, the discrepancy is probably due to remaining uncertainties in the opacities. Our H_2S line list is based on an ab initio calculation (R. Wattson 1995, private communication), which has not been compared to laboratory data in this part of the spectrum. The strong feature centered at 2.1084 μm is a blend of three strong lines from three different bands of H_2S. Possible errors in the position or strength of these lines could significantly reduce the amplitude of the feature in our synthetic spectra. The limitations of the background opacity of H_2O and CH_4 may also be responsible for the observed mismatch. Nevertheless, it is desirable to look for this feature at a higher resolution and a higher S/N as an absence of sulfur in Gl 229B would be a most intriguing result.

5.5. *Carbon Monoxide at* 4.7 μm

Given our determination of $T_{\rm eff}$ and $[M/H]$ in terms of the surface gravity, we can obtain the abundance of CO from the 4–5 μm spectra of Noll et al. (1997) and Oppenheimer et al. (1998), which are consistent with our results. For each model—A, B, and C—and using the metallicity given in Table 2, we computed synthetic spectra with various CO abundances. The latter is varied freely without imposing stoichiometric constraints. The synthetic spectra are binned to the wavelength grid of the data and fitted to the data by a normalization factor adjusted to minimize the χ^2. The χ^2 of the fitted spectra shows a well-defined minimum as a function of the CO abundance, $X_{\rm CO}$ (Table 3).

TABLE 3

ABUNDANCE OF CO FROM THE 4.7 μm BAND

Model	log g (cgs)	$T_{\rm eff}$ (K)	$[M/H]$	log $X_{\rm CO}$
A.....	4.5	870	−0.5	-4.0 ± 0.25
B.....	5.0	940	−0.3	-3.8 ± 0.3
C.....	5.5	1030	−0.1	-3.5 ± 0.3

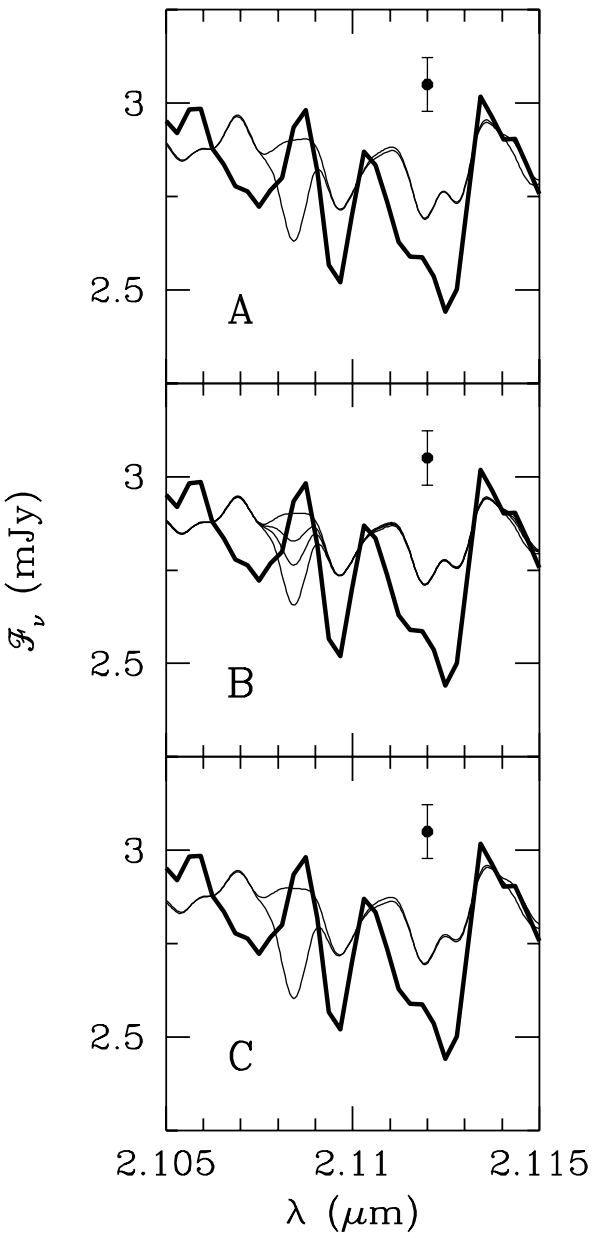

FIG. 17.—Hydrogen sulfide feature predicted at 2.1084 μm. The observed spectrum is shown by a heavy solid line. The thin lines in each panel show spectra computed for the indicated model (A, B, and C). Each spectrum is computed with the best-fitting metallicity for that model (Table 2). In each panel, the upper curve is calculated without H_2S opacity, and the lower curve is computed with the chemical equilibrium abundance of H_2S for the chosen metallicity. For model B (*middle panel*), the effect of reducing the equilibrium H_2S abundance by factors of 0.5 and 0.25, respectively, is also shown. All synthetic spectra are normalized to the data at 2.1062 μm, and the resolution is $R = 2800$.

The uncertainty on the CO abundance is obtained by generating synthetic data sets by adding a Gaussian distribution of the observed noise to the best fitting model spectrum. After doing the same analysis on 1000 synthetic data sets, we obtain a (non-Gaussian) distribution of values of X_{CO}. The uncertainties given in Table 3 correspond to the 68% confidence level. The Oppenheimer et al. (1998) spectrum gives CO abundances that are 0.1 dex higher than those obtained from the Noll et al. (1997) spectrum, which are well within the fitting uncertainty. Noll et al. (1997) found a CO mole fraction of 50–200 parts per million (ppm; $-4.3 \leq \log X_{CO} \leq -3.7$) by assuming a H_2O abundance of 300 ppm (effectively, $[M/H] = -0.6$), which agrees well with our result for model A, which has $[M/H] = -0.5$. Our results are also consistent with those of Griffith & Yelle (1999), who find CO abundances of ≥ 20 and ≥ 100 ppm ($\log X_{CO} \geq -4.7$ and -4) for $[M/H] = -0.6$ and 0, respectively, using the data of Noll et al. (1997).

Since this part of the spectrum contains only H_2O and CO features, our fitting procedure is sensitive only to the CO to H_2O abundance ratio. Chemical equilibrium calculations show that the H_2O abundance scales linearly with the metallicity at the level probed with 4–5 μm spectroscopy (i.e., all the gas-phase oxygen is in H_2O). Accordingly, the CO abundance we find scales with the metallicity of the model. As shown in Figure 18, the CO abundance determined from the 4.7 μm band corresponds approximately to the CO/CH_4 transition in chemical equilibrium. The observations definitely exclude the very low chemical equilibrium abundance of CO. The fact that the extreme case where all carbon is in CO provides an acceptable fit to the data (while we know that a good fraction of the carbon is in CH_4) is due to the rather noisy spectra.

6. DISCUSSION

6.1. *Surface Gravity*

It is highly desirable to restrict the surface gravity g of Gl 229B to an astrophysically useful range. Since L_{bol} is known, a determination of g fixes T_{eff}, the radius, the mass, and the age of Gl 229B (Fig. 4), as well as the metallicity and the abundances of important molecules such as CO and NH_3. The large uncertainty on g results in a large uncertainty in the mass of Gl 229B and on the age of the system determined from cooling tracks. While a dynamical determination of the mass may be possible in a decade or so (Golimowski et al. 1998), a spectroscopic determination might be obtained much sooner.

Unfortunately, it is not possible to constrain the gravity better than $\log g = 5 \pm 0.5$ with the data and models presently available. Our high-resolution spectroscopy does not allow us to choose between models A, B and C (Table 2) as an increase in gravity can be compensated by an increase in metallicity to lead to an identical fit. The gravity sensitivity of the K-band synthetic spectrum models reported by Burrows et al. (2000a) occurs for a fixed metallicity only.

Similarly, Allard et al. (1996) and Burrows et al. (2000a) report that the spectral energy distribution of Gl 229B models is fairly sensitive to the gravity. But this is true only for a fixed metallicity. For the three models indicated in Figure 4, and using the metallicity we have determined for each (Table 2), the gravity dependences of the infrared colors are $\Delta(H-K)/\Delta(\log g) = 0.03$ and $\Delta(J-K)/\Delta(\log g) = 0.03$ and $\Delta(K-L)/\Delta(\log g) = -0.08$ (Table 4). This dependence is very weak in the light of the uncertainty in the photometry of Gl 229B. More problematic is the fact that the synthetic $H-K$ disagrees with the photometry. Furthermore, the incomplete CH_4 opacities used in the spectrum calculation almost certainly result in an inaccurate redistribution of the flux in the near-infrared opacity windows that determine the broadband colors. An example of this effect on the H-band flux can be seen in Figure 10. We conclude that a photometric determination of the gravity is not possible at present.

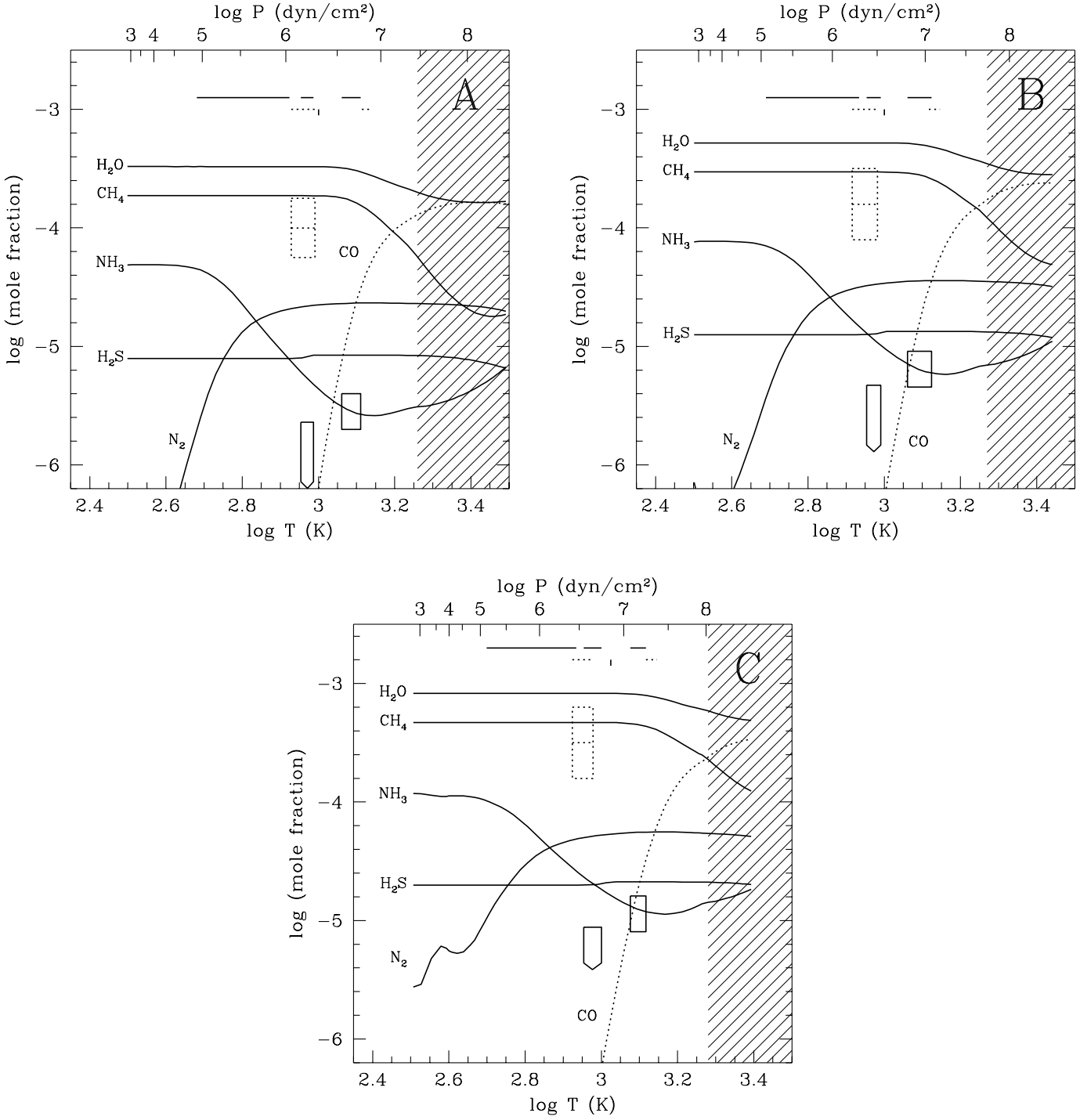

FIG. 18.—Equilibrium chemistry in the atmosphere of Gl 229B. The curves show the abundance of the important molecular species as a function of depth for each of the three gravities, computed with the metallicity we have determined for each (Table 2). Depth increases toward the right along the ordinate axis and is indicated by both temperature and pressure scales. The extent of the convection zone is shown by the shaded region. Horizontal bars at the top show the regions probed by spectroscopic observations of various molecular bands. The top row of solid bars shows three regions where NH_3 is detectable: 10 μm region and the K and H bands, from left to right, respectively. Dotted bars show the CO bands at 4.7 μm and in the H band, respectively. The vertical tick shows the depth where the 2.1084 μm feature of H_2S is formed. The dotted box shows the CO abundance determined from the at 4.7 μm band spectra of Noll et al. (1997) and Oppenheimer et al. (1998). Our determinations of the NH_3 abundance in the K an H bands are shown by vertical boxes, with the height of the box indicating the estimated uncertainty. For the K-band measurements, an arrow indicates that the NH_3 abundance could be close to zero. The labeling of the panels corresponds to the entries in Table 2.

An alternative approach to determining the gravity of Gl 229B is through a study of the pressure-broadened molecular lines of its spectrum. The spectrum of Gl 229B is formed of a forest of unresolved molecular lines mainly due to H_2O, CH_4, and NH_3. Because of the limitations of the CH_4 and NH_3 opacity databases, a detailed study of molecular features is best performed in spectral domains where these two molecules do not contribute significantly to the opacity.

TABLE 4

NEAR-INFRARED COLORS OF Gl 229B

Model	log g	$T_{\rm eff}$	[M/H]	$J-K$	$H-K$	$K-L'$
A	4.5	870	−0.5	−0.11	−0.27	2.25
B	5.0	940	−0.3	−0.14	−0.30	2.26
C	5.5	1030	−0.1	−0.08	−0.24	2.17
Leggett et al. 1999.....				-0.10 ± 0.07	-0.07 ± 0.07	2.24 ± 0.11

Spectroscopic observations with a resolution of $\sim 50{,}000$ can reveal the shape of individual H_2O lines in regions where they are relatively sparse, e.g., from 2.08 to 2.105 μm.

6.2. *Metallicity*

Our determination of the metallicity of Gl 229B, with an uncertainty of ± 0.1, is given in Table 2 for the three gravities considered. We find an excellent agreement between our three independent determinations of [M/H] for each gravity and conclude that Gl 229B is likely to be depleted in heavy elements, e.g., oxygen. The metallicity is near solar at high gravity and decreases significantly for lower gravities. In their analysis of the "red" spectrum, Griffith et al. (1998) found a H_2O abundance between 0.3 and 0.45 of the solar value for a $T_{\rm eff} = 900$ K, log $g = 5$ model, and they adopt a value of 0.25 in Griffith & Yelle (1999).

Metal depletion in Gl 229B is consistent with the analysis of the 0.985–1.02 μm FeH band in the spectrum of the primary star Gl 229A by Schiavon, Barbuy, & Singh (1997) who find [Fe/H] $= -0.2$. The infrared colors of Gl 229A imply that it is slightly metal rich, however (Leggett 1992). The relative metallicity of the components of this binary system may have been affected by their formation process. If the pair formed from the fragmentation of a collapsing cloud (like a binary star system), the two objects should share the same composition. If the brown dwarf formed like a planet, from accretion within a dissipative Keplerian disk around the primary, then the selective accretion of solid phase material could lead to an *enrichment* in heavy elements compared to the primary star, as is observed in the gaseous planets of the solar system. The low mass of the primary ($\sim 0.5\ M_\odot$) and the large semimajor axis and eccentricity ($a \gtrsim 32$ AU and $e \gtrsim 0.25$; Golimowski et al. (1998)) suggest that the binary formation process, and therefore equal metallicities, are more plausible. A more detailed study of the metallicity of Gl 229A is desirable for a better understanding of the history of this system.

6.3. *Atmospheric Chemistry and Molecular Abundances*

The results of our analysis of the metallicity and abundances of several molecules in the atmosphere of Gl 229B are summarized in Figure 18. Each panel corresponds to a different model (see Table 2) and shows the abundances of important molecules as a function of depth in the atmosphere based on chemical equilibrium calculations including condensation cloud formation. The chemistry of these abundant molecules is fairly simple. The abundance of H_2O is uniformly reduced by $\sim 16\%$ by silicate condensation. Except for a small depletion for log $T \lesssim 3$ due to the condensation of Na_2S, all sulfur is found in H_2S. The other molecules shown are not affected by condensation. Nitrogen is partitioned between N_2 and NH_3, with the latter being favored at lower temperatures and higher pressures. NH_3 dominates near the surface and rapidly transforms into N_2 at the higher temperatures found deeper in the atmosphere. Deep in the atmosphere, the higher pressures cause a partial recombination of NH_3 and the ratio of the NH_3 to N_2 abundances increases slowly with depth. In a similar fashion, all elemental carbon is found in CH_4 at the surface but CO starts to form at higher temperatures and rapidly becomes the most abundant carbon-bearing molecule. The formation of CO consumes H_2O, as can be seen in Figure 18.

In each panel, a dotted box indicates the CO abundance we have determined from the 4.7 μm spectrum; the location of the box along the abscissa shows the level probed at this wavelength (Fig. 6). As originally discussed by Noll et al. (1997) and Griffith & Yelle (1999), the CO abundance is ~ 3 orders of magnitude larger than the chemical equilibrium value. Stoichiometric constraints imply that this also results in a significant reduction of the CH_4 abundance at the 870–950 K level in Gl 229B. In model B, the equilibrium abundance of CH_4 at 900 K is 2.97×10^{-4}, which corresponds to the abundance of elemental carbon. The CO abundance determined from the 4.7 μm band is 1.6×10^{-4} (with a large error bar). Conservation of the total number of carbon atoms then requires that the CH_4 abundance be $\sim 1.4 \times 10^{-4}$, a full factor of 2 below the equilibrium abundance. If we use the lowest CO abundance allowed by our analysis, a 25% reduction of CH_4 relative to its equilibrium abundance at 900 K results. Depletion of CH_4 at this depth is readily accessible spectroscopically in the 1.6 and 3.3 μm bands and may also affect the 2.3 μm band if the nonequilibrium CO abundance persists at higher levels (Fig. 6). After H_2O, CH_4 is the most important near-infrared molecular absorber in Gl 229B. Accurate modeling of the spectrum demands a careful treatment of the nonequilibrium CH_4 abundance.

Similarly, solid boxes show the NH_3 abundance determined from our H- and K-band spectra. While the H-band abundance is in excellent agreement with the equilibrium value, there is a clear depletion of NH_3 in the K band. The H- and K-band abundances are marginally consistent with each other, but it appears that the NH_3 abundance decreases upward through the atmosphere.

6.4. *Nonequilibrium Processes*

Processes that take place faster than the timescale of key chemical reactions can drive the composition of the mixture away from equilibrium. The case of CO/CH_4 chemistry has been well studied in the atmosphere of Jupiter, where an overabundance of CO is also observed. Carbon monoxide is a strongly bound molecule, and the conversion of CO to CH_4 through the (schematic) reaction

$$CO + 3H_2 \rightarrow CH_4 + H_2O \qquad (2)$$

proceeds relatively slowly, while the reverse reaction is much faster. Vertical transport, if vigorous enough, can

carry CO-rich gas from deeper levels upward faster than the CO to CH_4 reaction can take place. The CO/CH_4 ratio at any level is fixed ("quenched") by the condition

$$\tau_{\rm chem} = \tau_{\rm mix} , \quad (3)$$

where $\tau_{\rm chem}$ is the chemical reaction timescale and $\tau_{\rm mix}$ the dynamical transport timescale. Wherever $\tau_{\rm mix} \leq \tau_{\rm chem}$ in the presence of a vertical gradient in the equilibrium abundance, nonequilibrium abundances will result.

As discussed by Fegley & Lodders (1996), Noll et al. (1997), Griffith & Yelle (1999), and references therein, this naturally explains the very high CO abundance observed at the 900 K level. In this picture, CO-rich gas would be carried upward from $T \gtrsim 1400$ K. Convection is the most obvious form of vertical transport in a stellar atmosphere, but in Gl 229B the convection zone remains about 3 pressure scale heights below the level where CO is observed (*shaded area* in Fig. 18). Perhaps convective overshooting can transport CO to the observed level. Griffith & Yelle (1999) propose "eddy diffusion" as a slower but adequate transport mechanism. The eddy diffusion (or mixing) timescale is constrained by the poorly known CO abundance and the somewhat uncertain chemical pathway between CO and CH_4. From Griffith & Yelle (1999), we infer that $\tau_{\rm mix} \lesssim$ 1–10 yr and could be much smaller.

In analogy to the CO/CH_4 equilibrium, a low NH_3 abundance can be explained by vertical transport, which can quench the NH_3/N_2 ratio at a value found in deeper layers in the atmosphere. As it is carried upward, N_2 is converted to NH_3 by the reaction

$$N_2 + 3H_2 \rightarrow 2NH_3 . \quad (4)$$

The N_2 molecule is very strongly bound, however, and this reaction proceeds extremely slowly at low temperatures, much more slowly than reaction (2). Thermochemical kinetic calculations of the chemical lifetime for conversion of N_2 to NH_3 were performed as described in Fegley & Lodders (1994). The timescale for reaction (4) along the (P, T) profiles of models A, B, and C and for $P > 1$ bar is given by

$$\log \tau_{\rm chem} = \frac{3.75 \times 10^4}{T} + 0.22 \log g - 23.08 , \quad (5)$$

where $\tau_{\rm chem}$ is in years, T is the temperature in kelvins, and g is the surface gravity in centimeters per square second. This timescale assumes that the N_2 conversion occurs in the gas phase, although it could possibly be shortened by catalysis on the surface of grains. The timescale increases very steeply with decreasing temperature. At the level probed in the H band, $\log T = 3.1$ and $\log \tau_{\rm chem} = 7.8$, and, in the K band, $\log T = 2.95$ and $\log \tau_{\rm chem} = 20.1$! At some intermediate level (which depends on g), the timescale for the conversion of N_2 into NH_3 becomes longer than the age of Gl 229B. In view of the relatively very short mixing timescale inferred from the CO abundance, it follows that the NH_3 abundance in the H and K bands is *entirely* determined by nonequilibrium processes, *not* by reaction (4). At depths where $\log T > 3.23$ (which corresponds to the top of the convection zone), $\tau_{\rm chem} < 1$ yr and the reaction proceeds fast enough to establish chemical equilibrium between NH_3 and N_2. We therefore expect that the N_2/NH_3 ratio will be quenched at its value at $\log T \approx 3.23$ throughout the remainder of the atmosphere. While the timescale for eddy diffusion increases in the upper levels of the atmosphere, the extremely long $\tau_{\rm chem}$ ensures that the NH_3/N_2 ratio remains unchanged, regardless of how slowly the vertical mixing proceeds. For model B, this corresponds to $\log X_{\rm NH_3} = -5.2$, in perfect agreement with the abundance found in the H band (Fig. 18*b*).

While the abundance of NH_3 determined from the K-band spectrum is not very precise, it is marginally consistent with vertical mixing. Figure 18 shows that it is more likely that the K-band abundance is smaller than found in the H band, however. On the other hand, the abundances shown in Figure 18 and Table 2 are depletion factors that were applied uniformly to the chemical equilibrium abundance profile of NH_3, which has a large vertical gradient. For consistency with the mixed atmosphere picture, we have therefore redetermined NH_3 abundances using a constant abundance throughout the atmosphere and found $\log X_{\rm NH_3} \leq -5.0$ and -4.7 ± 0.15 from the K- and H-band spectra, respectively (model B). The former is in good agreement with our simple prediction, while the H-band value is now rather high. The discrepancy between the H- and K-band results thus persists in this new analysis. Changes in $[M/{\rm H}]$ within the ± 0.1 uncertainty also have little effect.

We consider the possibility that this vertical gradient in the NH_3 abundance may be caused by a different nonequilibrium process such as the photolysis of NH_3 by the UV flux from the primary star. Ammonia is a relatively fragile molecule that is easily dissociated by UV photons:

$$NH_3 + h\nu \rightarrow NH_2 + H . \quad (6)$$

With a photodissociation cross section of $\approx 6 \times 10^{-18}$ cm^2 per molecule, optical depth unity for the photodissociation of NH_3 is reached at pressures of a few millibars in Gl 229B. Photodissociation of the much more abundant H_2 molecules does not effectively shield NH_3 from incoming UV photons since the two molecules absorb over different wavelength ranges. Photodissociation of NH_3 therefore represents a net sink of NH_3 that occurs at the very top of the atmosphere. We can estimate a lower limit to the timescale of photodissociation of NH_3 by assuming that each photodissociating photon results in the destruction of a NH_3 molecule. The incident photon flux is

$$N_{\rm UV} = \left(\frac{R_*}{d}\right)^2 \int_{\lambda_0}^{\lambda_1} \frac{\lambda \mathscr{F}_\lambda}{hc} \, d\lambda \approx \left(\frac{R_*}{d}\right)^2 \frac{\bar{\lambda} \mathscr{F}_{\bar{\lambda}}}{hc} \, \Delta\lambda , \quad (7)$$

where photons causing dissociation of NH_3 are between λ_0 and λ_1, $\mathscr{F}_\lambda$ is the flux at the surface of the primary star, R_* the radius of the primary star, and d the separation of the binary system. For NH_3, we have $\bar{\lambda} \sim 1900$ Å and $\Delta\lambda \sim 300$ Å (J. Moses 1999, private communication). The primary star has a dM1 spectral type, with $\mathscr{F}_{\bar{\lambda}} \sim 10^7$ ergs cm^{-2} s^{-1} cm^{-1} and $R_* \sim 3.6 \times 10^{10}$ cm (Leggett et al. 1996). The binary separation is $d \gtrsim 44$ AU (Golimowski et al. 1998). This results in $N_{\rm UV} \lesssim 8.3 \times 10^3$ cm^{-2} s^{-1}. Photodissociation will affect significantly the NH_3 abundance when

$$\tau_{\rm phot} = \frac{\sigma}{N_{\rm UV}} \lesssim \tau_{\rm mix} , \quad (8)$$

where σ is the column density of NH_3. Because the incident flux of UV photons is fairly low, this condition is satisfied only at pressures below a few microbars, i.e., very high in

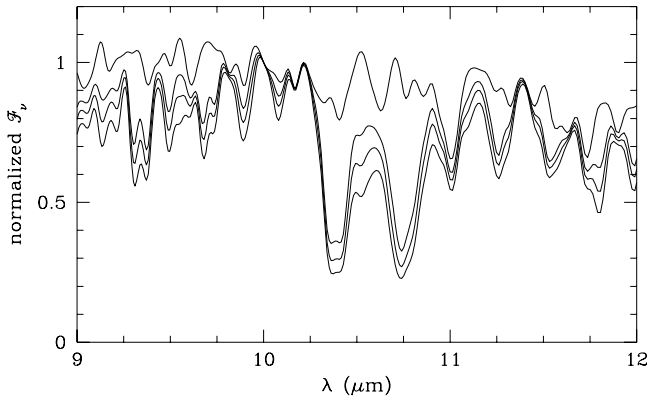

FIG. 19.—Ammonia features in the 10 μm region. The spectra are computed with model B and $[M/H] = -0.4$. Each curve corresponds to a different depletion of NH_3 relative to its equilibrium abundance, with the abundance of all other compounds being kept the same. The equilibrium abundance of NH_3 has been multiplied by 0, 0.25, 0.5, and 1, from top to bottom, respectively. All spectra are normalized at 10 μm, and the resolution is $R = 200$.

the atmosphere. In the region of interest, photodissociation destroys a very small fraction of NH_3 during one mixing timescale and therefore has little effect on the abundance of NH_3. Photolysis of NH_3 cannot explain the relatively low NH_3 abundance we find in the K-band spectrum.

We believe that the difference between the H- and K-band determinations of the NH_3 abundance arises from the limitations of the NH_3 opacity data used for the calculation of the synthetic spectra. As discussed above, the incompleteness of the NH_3 line list for $T > 300$ K results in upper limits for the NH_3 abundances obtained by fitting the data. Since this effect increases with temperature, we expect that the abundance determined from the H-band spectrum is overestimated relative to the one obtained from the K-band spectrum, which is what we observe. Until NH_3 opacities become available for $T \sim 800$–1200 K, we will not be able to quantify this effect.

Figures 6 and 18 show that ammonia offers a third window of opportunity for a determination of its abundance. The region between 8.3 and 14.4 μm is rich in strong NH_3 features, the two strongest being at 10.35 and 10.75 μm (Fig. 19). This spectral region probes a higher level in the atmosphere ($T \sim 500$–800 K), where the hot bands of NH_3 that are missing from opacity data bases are less problematic than in the H and K bands. In this spectral region, the spectrum is very sensitive to the NH_3/H_2O ratio, especially for NH_3 abundances below 25% of the equilibrium value (Fig. 19). This would allow a good determination of the degree of NH_3 depletion in the upper levels of the atmosphere. We anticipate that 10 μm spectroscopy should reveal a NH_3 abundance of $\lesssim 10\%$ of its equilibrium value.

7. CONCLUSION

With the availability of extensive photometric, astrometric, and spectroscopic data, our picture of the atmosphere of Gl 229B is gradually becoming more exotic and more complex. The initial discovery of CH_4 in its spectrum set it apart and has prompted the creation of a new spectral class, the T dwarfs. H_2O, CO, Cs I, and K I have also been detected. There is good evidence that the rapid decrease of the flux at visible wavelengths is caused by unprecedently broad lines of atomic alkali metals (Liebert et al. 2000). The presence of condensates may also play a role in shaping the spectrum of Gl 229B.

It is unfortunate that the surface gravity of Gl 229B remains poorly constrained. We have not been able to restrict the allowed range further with our new J, H, and K spectroscopy. As a result, all our results are expressed as a function of gravity. This is the most significant obstacle to further progress in elucidating the astrophysics of this T dwarf. The surface gravity can probably be determined from the study of the pressure broadened shape of molecular lines.

We have found good evidence for the presence of NH_3 in the spectrum of Gl 229B, which was expected from chemical equilibrium calculations. We have been able to determine its abundance at two different levels in the atmosphere, and we find a significant deviation from chemical equilibrium. A similar situation has been previously found with CO (Noll et al. 1997), and this abundance pattern can be explained by vertical mixing in the atmosphere. The extent of the convection zone is not sufficient to account for the abundances we find, and the mixing may be due to overshooting or to less efficient eddy diffusion. We find that NH_3 photolysis is not important in shaping the spectrum of Gl 229B. Because NH_3 can be observed in three different bands corresponding to three distinct depths in the atmosphere, an accurate determination of its abundance in each band provides information on the timescale of mixing as a function of depth. This is an unusual and powerful diagnostic tool that can provide valuable clues for modeling the vertical distributions of possible condensates. In principle, any absorber with a large abundance gradient through the visible part of the atmosphere can be used to infer the details of the mixing process. Among detected and abundant molecules, only CO and NH_3 satisfy this criterion. Chemical equilibrium calculations with rainout of condensates (Lodders 1999; Burrows et al. 2000b) show that we can expect significant vertical gradients in the abundances of atomic K, Rb, Cs, and Na as they become bound in molecules (KCl, RbCl, CsCl, and Na_2S, respectively) in the cooler, upper reaches of the atmosphere. Cesium and potassium have been detected in the spectrum of Gl 229B, and resonance doublets of K I and Na I appear to shape the visible spectrum. However, the chemical timescales for alkali metals are so short that they should always remain in thermodynamic equilibrium (Lodders 1999). Therefore, they cannot serve as probes of vertical mixing in Gl 229B.

Further progress in understanding the atmosphere of Gl 229B requires better opacities for CH_4 and NH_3, and, to a lesser extent, for H_2O. A more accurate determination of the CO abundance from 4–5 μm spectroscopy is very desirable and will require higher S/N spectroscopy than is currently available. Similarly, 10 μm spectroscopy to determine the NH_3 abundance for $P \lesssim 1$ bar, while difficult, is important.

The issue of vertical mixing and departures from chemical equilibrium gains importance when we consider that the observed departure of CO from chemical equilibrium implies a significantly reduced CH_4 abundance, by conservation of the abundance of elemental carbon. Similarly, our results imply that NH_3 absorption in the 10 μm region is reduced. Because CH_4 is a significant absorber in the near-infrared, as is NH_3 in the 10 μm range, departures from equilibrium must be taken into account when accurate

modeling of the atmosphere and spectrum of Gl 229B is desired. This new level of complexity compounds the exoticism and the challenges posed by T dwarfs.

The astrophysics of Gl 229B is far richer than has been originally anticipated. Gl 229B is currently the only T dwarf known to be in a binary system. There is no evidence that the illumination from the primary star has a significant effect on the state of its atmosphere, and Gl 229B is most likely typical of isolated T dwarfs. It remains the brightest and by far the best studied of the seven T dwarfs currently known, but the list should expand to several dozen during the next 2–3 years (Burgasser et al. 1999; Strauss et al. 1999). The existing body of work on Gl 229B points to the most rewarding observations to conduct on T dwarfs. The possibility of studying trends in the physics of T dwarf atmospheres as a function of effective temperature is a fascinating prospect.

We thank T. Guillot for sharing programs that were most useful to our analysis, J. Moses for invaluable information regarding the photolysis of NH_3 in giant planets, and K. Noll and B. Oppenheimer for sharing their data. We are grateful to the staff at the United Kingdom Infrared Telescope, which is operated by the Joint Astronomy Center Hawaii on behalf of the UK Particle Physics and Astronomy Research Council. This work was supported in part by NSF grants AST-9318970 and AST-962487 and NASA grants NAG5-4988 and NAG5-4970. Work by B. Fegley and K. Lodders is supported by grant NAG5-6366 from the NASA Planetary Atmospheres Program.

REFERENCES

Allard, F., Hauschildt, P. H., Baraffe, I., & Chabrier, G. 1996, ApJ, 465, L123
Bohren, C. F., & Huffman, D. R. 1983, Absorption and Scattering of Light by Small Particles (Wiley: New York)
Burgasser, A. J., et al. 1999, ApJ, 522, L65
Burrows, A., Hubbard, W. B., Lunine, J. I., Marley, M. S., & Saumon, D. 2000a, in Protostars and Planets IV, ed. V. Mannings, A. Boss, & S. S. Russell (Tucson: Univ. Arizona Press) 1339
Burrows, A., Marley, M. S., & Sharp, C. 2000b, ApJ, 531, 438
Burrows, A., & Sharp, C. M. 1999, ApJ, 512, 843
Burrows, A., et al. 1997, ApJ, 491, 856
Fegley, B., Jr., & Lodders, K. 1994, Icarus, 110, 117
———. 1996, ApJ, 472, L37
Fegley, B., Jr., & Prinn, R. G. 1988, ApJ, 324, 621
Geballe, T. R., Kulkarni, S. R., Woodward, C. E., & Sloan, G. C. 1996, ApJ, 467, L101
Golimowski, D. A., Burrows, C. J., Kulkarni, S. R., Oppenheimer, B. R., & Brukardt, R. A. 1998, AJ, 115, 2579
Griffith, C. A., & Yelle, R. A. 1999, ApJ, 519, L85
Griffith, C. A., Yelle, R. A., & Marley, M. S. 1998, Science, 282, 2063
Guillot, T. 1999, Science, 286, 72
Husson, N., Bonnet, B., Scott, N. A., & Chedin, A. 1992, J. Quant. Spectrosc. Radiat. Transfer, 48, 509
Karkoschka, E. 1994, Icarus, 111, 174
Kirkpatrick, J. D., et al. 1999, ApJ, 519, 834
Leggett, S. K. 1992, ApJS, 82, 351
Leggett, S. K., Allard, F. Berriman, G., Dahn, C. C., & Hauschildt, P. H. 1996, ApJS, 104, 117
Leggett, S. K., Toomey, D. W., Geballe, T. R., & Brown, R. H. 1999, ApJ, 517, L139
Liebert, J., Reid, I. N., Burrows, A., Burgasser, A. J., Kirkpatrick, J. D., & Gizis, E. 2000, ApJ, 533, L155
Lodders, K. 1999, ApJ, 519, L793
Marley, M. S., Saumon, D., Guillot, T., Freedman, R. S., Hubbard, W. B., Burrows, A., & Lunine, J. I. 1996, Science, 272, 1919
Matthews, K., Nakajima, T., Kulkarni, S. R., & Oppenheimer, B. R. 1996, AJ, 112, 1678
Mountain, C. M., Robertson, D. J., Lee, T. J., & Wade, R. 1990, Proc. SPIE, 1235, 25
Nakajima, T., Oppenheimer, B. R., Kulkarni, S. R., Golimowski, D. A., Matthews, K., & Durrance, S. T. 1995, Nature, 378, 463
Noll, K. S., Geballe, T. R., & Marley, M. S. 1997, ApJ, 489, L87
Oppenheimer, B. R., Kulkarni, S. R., Matthews, K., & Nakajima, T. 1995, Science, 270, 1478
Oppenheimer, B. R., Kulkarni, S. R., Matthews, K., & van Kerkwijk, M. H. 1998, ApJ, 502, 932
Partridge, H., & Schwenke, D. W. 1997, J. Chem. Phys., 106, 4618
Perryman et al. 1997, A&A, 323, L49
Rothman, L. S., et al. 1998, J. Quant. Spectrosc. Radiat. Transfer, 60, 665
Schiavon, R. P., Barbuy, B., & Singh, P. D. 1997, ApJ, 484, 499
Schultz, A. B., et al. 1998, ApJ, 492, L181
Strauss, M. A., et al. 1999, ApJ, 522, L61
Strong, K., Taylor, F. W., Calcutt, S. B., Remedios, J. J., & Ballard, J. 1993, J. Quant. Spectrosc. Radiat. Transfer, 50, 363
Tsuji, T., Ohnaka, K., & Aoki, W. 1999, ApJ, 520, L119
Tsuji, T., Ohnaka, K., Aoki, W., & Nakajima, T. 1996, A&A, 308, L29